



JGR Space Physics



RESEARCH ARTICLE

10.1029/2023JA031455

Key Points:

- We present results from an experimental campaign designed to monitor the dynamics of sporadic-E layers
- Our observations are consistent with the wind-shear theory and show that zonal shears play an important role at lower altitudes
- We find sporadic-E can significantly alter HF communication links and likely enable near-range communications

Supporting Information:

Supporting Information may be found in the online version of this article.

Correspondence to:

B. S. R. Kunduri, bharatr@vt.edu

Citation:

Kunduri, B. S. R., Erickson, P. J., Baker, J. B. H., Ruohoniemi, J. M., Galkin, I. A., & Sterne, K. T. (2023). Dynamics of mid-latitude sporadic-E and its impact on HF propagation in the North American sector. *Journal of Geophysical Research: Space Physics*, 128, e2023JA031455. https://doi.org/10.1029/2023JA031455

Received 3 MAR 2023 Accepted 4 SEP 2023

© 2023. The Authors.

This is an open access article under the terms of the Creative Commons Attribution-NonCommercial License, which permits use, distribution and reproduction in any medium, provided the original work is properly cited and is not used for commercial purposes.

Dynamics of Mid-Latitude Sporadic-E and Its Impact on HF Propagation in the North American Sector

B. S. R. Kunduri¹, P. J. Erickson², J. B. H. Baker¹, J. M. Ruohoniemi¹, I. A. Galkin³, and K. T. Sterne¹

¹Bradley Department of Electrical and Computer Engineering, Virginia Tech, Blacksburg, VR, USA, ²Haystack Observatory, Massachusetts Institute of Technology, Westford, MA, USA, ³Space Science Laboratory, University of Massachusetts, Lowell, MA, USA

Abstract Sporadic-E (Es) are thin layers of enhanced ionization observed in the E-region, typically between 95 and 120 km altitude. Es plays an important role in controlling the dynamics of the upper atmosphere and it is necessary to understand the geophysical factors influencing Es from both the scientific and operational perspectives. While the wind-shear theory is widely accepted as an important mechanism responsible for the generation of Es, there are still gaps in the current state of our knowledge. For example, we are yet to determine precisely how changes in the dynamics of horizontal winds impact the formation, altitude, and destruction of Es layers. In this study, we report results from a coordinated experimental campaign between the Millstone Hill Incoherent Scatter Radar, the SuperDARN radar at Blackstone, and the Millstone Hill Digisonde to monitor the dynamics of mid-latitude Es layers. We report observations during a 15-hr window between 13 UT on 3 June 2022 and 4 UT on 4 June 2022, which was marked by the presence of a strong Es layer. We find that the height of the Es layer is collocated with strong vertical shears in atmospheric tides and that the zonal wind shears play a more important role than meridional wind shears in generating Es, especially at lower altitudes. Finally, we show that in the presence of Es, SuperDARN ground backscatter moves to closer ranges, and the height and critical frequency of the Es layer have a significant impact on the location and intensity of HF ground scatter.

1. Introduction

Sporadic-E (Es) are vertically thin layers of enhanced metallic ionization that form in the E region of the ionosphere. Es are usually observed between 95 and 120 km altitude (Haldoupis, 2011), and have a typical thickness of ~1–2 km in altitude (Zeng & Sokolovskiy, 2010). While Es layers have a small vertical extent, they have a large horizontal scale, reaching several hundred kilometers (Arras et al., 2008; Cathey, 1969; Maeda & Heki, 2015; Wu et al., 2005). A few previous studies have examined the zonal and meridional extent of Es layers to determine their 2d shape and structure. A few previous studies (e.g., Hysell et al., 2009; Larsen et al., 2007; Maeda & Heki, 2014, 2015) have examined the morphology of Es layers to determine their 2d shape and structure. Using a coherent scatter radar, Hysell et al. (2009) showed the existence of horizontal structures of field-aligned irregularities embedded in Es that are elongated in the east-west and northwest-southeast directions. Later, Maeda and Heki (2014) used Total Electron Content (TEC) observations from a dense network of Global Positioning System (GPS) receivers in Japan and showed Es were composed of frontal structures extending over 100 km in the eastwest direction. Further extending the analysis of Es using GPS TEC, Maeda and Heki (2015) analyzed more than 70 events in the Japanese sector and found that Es patches were characterized by an azimuthal frontal structure elongated in the east-west direction, reaching a scale size of ~100 km. Electron densities in Es layers exceed those usually observed in the E-region of the ionosphere, and at times can even exceed the peak electron densities of the F-region (Haldoupis, 2011; Whitehead, 1989). A few previous studies have demonstrated that critical frequencies of the Es layer (foEs) can exceed 20 MHz (Chandra & Rastogi, 1975; Chartier et al., 2022). Previous studies investigating Es have predominantly relied on measurements from ionosondes (e.g., Rawer, 1949; Matsushita & Reddy, 1967; Merriman et al., 2021), Incoherent Scatter Radars (ISRs) (e.g., Christakis et al., 2009; Hysell et al., 2018; Larsen, 2000), sounding rockets (Smith, 1966), and GPS Radio Occultation (RO) techniques (Arras et al., 2008; Arras & Wickert, 2018; Chu et al., 2014; Hodos et al., 2022; Wu et al., 2005). GPS-RO based techniques showed wide variation in occurrence rates of Es with the inconsistency attributed to differences in intensity thresholds for Es used by these studies (Carmona et al., 2022). A new methodology was developed by

KUNDURI ET AL. 1 of 14

Obenberger et al. (2021) to monitor Es over a large geographical region using the long wavelength array telescopes in New Mexico.

Es layers can have a significant impact on radio wave propagation. For example, High Frequency (HF), and Very High Frequency (VHF), radio waves can experience refraction and reflection associated with Es density gradients (Cameron et al., 2022; Chartier et al., 2022). Es might open new modes of propagation by altering the reflection height of HF and VHF waves, sometimes enabling long distance multi-hop propagation. In other cases, Es might blanket the ionosphere preventing the ability to remote sense the ionosphere at higher altitudes. Ham radio operators have long used Es for long-range communications. Lastly, Es occurrence has been shown to be correlated with the generation of MSTIDs on the night-side (Otsuka et al., 2008). Es is thought to impact magnetosphere-ionosphere coupling by altering ionospheric conductivity and electrodynamics. It is therefore important to understand the mechanisms generating and influencing Es from the scientific as well as the radio-wave communications perspective.

The most widely accepted theory for the formation of Es at mid-latitudes is the wind shear theory, proposed initially by Whitehead (1961) and Axford (1963). Over the next several decades the wind shear theory was further developed and tested by several researchers (e.g., Haldoupis, 2011; Mathews, 1998; Shinagawa et al., 2021; Yamazaki et al., 2022). In brief, the wind shear theory hypothesizes that thin layers of enhanced ionization can form in the dynamo region of the ionosphere due to vertical shears in the horizontal neutral wind. For example, in the Northern hemisphere, a westward (northward) zonal (meridional) wind at higher altitudes and an eastward (southward) wind at lower altitudes cause the ions to drift downwards from above and upwards from below due to the Lorentz force. As a result, the ions converge where the shear is null (e.g., Chimonas & Axford, 1968; Haldoupis, 2011). An expression for the vertical ion velocity assuming a balance between Lorentz force and frictional force due to ion-neutral collisions can be given as (e.g., Haldoupis, 2011; Yamazaki et al., 2022):

$$w_{i} = \frac{\frac{v_{i}}{\omega_{i}}U\cos I - V\cos I\sin I}{1 + \left(\frac{v_{i}}{\omega_{i}}\right)^{2}} \tag{1}$$

In Equation 1, w represents the vertical ion speed, V is meridional wind (+north), U is zonal wind (+east), I is geomagnetic dip angle, ν_i is the ion-neutral collision frequency, and ω_i is the ion gyrofrequency. Es layers are expected to form at altitudes where the ions converge. In other words, mathematically, conditions are favorable for the formation of Es when $\frac{\partial w_i}{\partial z}$ < 0. Observations from the ISR at Arecibo showed that the diurnal, semidiurnal, and terdiurnal tides can play an important role in the formation of Es (Haldoupis et al., 2004). It can further be noted from Equation 1 that the degree of ion convergence produced by U and V not only depends on the vertical shears/gradients, but also on $\frac{v_i}{\omega_i}$. Since $\frac{v_i}{\omega_i}$ varies with altitude, the relative contribution of U and V in producing ion convergence is also expected to change with altitude. Another factor that provides important clues about Es generation is the composition of these layers. Since Es have a lifespan of several hours (Bishop & Earle, 2003), the wind shear theory is not compatible with ambient ions which have short lifespans since they neutralize in a few minutes via dissociative recombination (Haldoupis, 2011). It was therefore suggested that Es layers could be composed of metallic ions which undergo slow radiative recombination and therefore have longer lifetimes (Mathews, 1998; Whitehead, 1989). Observations using rocket campaigns have shown that Es layers do in fact result from the ionization of metal atoms of meteoric origin such as Fe+ and Mg+ (Kopp, 1997). Using observations from a series of NASA sounding rockets launched from Wallops Island, VA, Roddy et al. (2007) showed that metallic ions may be a significant source of ionization in the nighttime E and F region ionosphere at mid-latitudes.

A key characteristic of Es is the strong seasonal dependence, marked by a pronounced increase in their occurrence rate during Summer (Arras et al., 2008; Chu et al., 2014). Earlier studies have shown that Es occurrence rate and intensity maximize during June–July and December–January for the northern and southern hemispheres, respectively (Whitehead, 1989, & references therein). The windshear theory cannot fully explain this seasonal variability in Es occurrence. In particular, it cannot account for the pronounced summer maximum in Es occurrence (Haldoupis, 2011). The strong seasonal variability in Es occurrence has remained a topic of active research. Two competing theories have emerged to explain the summer maximum in Es occurrence. The first theory attributes the summer maximum in Es occurrence rates to a similar increase in daily meteor count rates during summer (Lau et al., 2006; Singer et al., 2004). This seasonal variability in meteor counts was attributed to the fact that

KUNDURI ET AL. 2 of 14

21699402, 2023, 9, Downloaded from https

s://agupubs.onlinelibrary.wiley.com/doi/10.1029/2023JA031455, Wiley Online Library on [11/07/2024]. See the Terms

meteor radiants arrive from well-defined sources located near the ecliptic plane and therefore favor the summer hemisphere. It was suggested that the larger meteor deposition rate provided the metallic ions which constitute Es layers (Feng et al., 2013; Haldoupis et al., 2007). However, Janches et al. (2006) presented contradictory observations suggesting meteor deposition rates peak during autumn months (September in the northern hemisphere), and not necessarily in summer. A second alternative mechanism was later suggested by Yu et al. (2021) which attributed the seasonal variability in Es occurrence to a global-scale winter-to-summer transport of metallic ions in the upper atmosphere. The monthly Es occurrence rates reported by Hodos et al. (2022) supported the second theory. Overall, the seasonal variability in Es occurrence and intensity is an active area of research and not fully understood.

In this study, we present a focused observational study of sporadic E using results from coordinated E-layer experiments between Millstone Hill ISR, the Blackstone (BKS) SuperDARN, and the Millstone Hill Digisonde DPS-4D. A key difference between our experimental campaign and previous studies that relied on rocket observations (e.g., Hall et al., 1971) or GPS radio occultation measurements (e.g., Chu et al., 2014; Yamazaki et al., 2022) is that we monitor Es and tidal motion continuously over several hours. Our observations therefore provide an opportunity to examine the dynamics and evolution of Es in response to changes in tidal motion. We compare observations of tidal motion from the ISR with the intensity and occurrence of Es derived from ionosonde observations, and also with meteor backscatter observed by SuperDARN to analyze the sources generating Es.

2. Data Sets

2.1. SuperDARN

SuperDARN is a global network of HF radars making backscatter measurements over large geographical regions in both the Northern and the Southern Hemispheres (Chisham et al., 2007; Nishitani et al., 2019). The Blackstone SuperDARN radar (BKS) has been used in the current study to analyze the impact of meteor scatter in the formation of Es, and also to determine the impact of Es on HF propagation. The BKS radar is located in Blackstone, VA (37.10°N, -77.95°E). Beam-22 of the BKS radar is closest to Millstone Hill and is particularly suitable for running experimental campaigns that require closely coincident measurements. The BKS radar typically scans through 24 beams, covering an azimuth of ~50° with a temporal resolution of 1–2 min. Backscatter from Super-DARN radars typically originates from: (a) decameter scale magnetic field aligned plasma irregularities in the E and F regions of the ionosphere (Ruohoniemi et al., 1987), (b) ground or sea reflections, and (c) meteor trails left by meteoroids entering the Earth's atmosphere (Hall et al., 1997). The primary SuperDARN observables are signal-to-noise ratio, line-of-sight (LoS) Doppler velocity, and width of the Doppler spectrum (spectral width). The location of ground scatter and the number of near-range meteor scatter echoes observed by the BKS radar will be analyzed in this study.

2.2. Millstone Hill Incoherent Scatter Radar

The goals of this study are to determine the relationship between Es and atmospheric tides at mid-latitudes and to test the wind-shear theory. We will primarily analyze measurements from the MISA 46 m steerable antenna of the Millstone Hill ISR, part of the NSF Millstone Hill Geospace Facility at Westford, MA (42.619°N/288.508°E). The MISA look direction was pointing southwest (-120° azimuth), toward the BKS radar, with a low elevation angle of 30° reaching the E-region at a range of 200 km. The altitude resolution in the E-region for this experiment was \sim 1.3 km, similar to the vertical thickness of Es structures (Zeng & Sokolovskiy, 2010). The ISR was activated \sim 1300 UT on 3 June 2022 and the experiment concluded \sim 0400 UT the next day. A 16 baud strong alternating code (Lehtinen & Häggström, 1987) with 30 µsec bauds was used. The two main parameters of interest in this study are MISA measurements of electron density and LoS ion velocity. It is noteworthy that at altitudes below \sim 110–120 km, ion-neutral collisions are frequent enough that ions move with neutrals and can be used as direct tracers for neutral winds (Evans, 1972a, 1972b, 1978) and atmospheric tides.

A summary of the coordinated experimental campaign is presented in Figure 1, which shows a map in geographic coordinates showing the fields-of-view of the BKS radar. The location of the Millstone Hill ionosonde is also overlaid on the plot as a blue dot. The red arc indicates the region where Millstone Hill ISR's MISA antenna can monitor the E-region at 30° elevation and 200 km range. We note from Figure 1 that the eastern most BKS beam does not look directly over the location where MISA is making observations in the E-region. Given the typical

KUNDURI ET AL. 3 of 14

21699402, 2023, 9, Downloaded from https://agupubs.onlinelibrary.wiley.com/doi/10.1029/2023JA031455, Wiley Online Library on [11/07/2024]. See the Terms

and-conditions) on Wiley Online Library for rules of use; OA articles are governed by the applicable Creative Commons Licenso

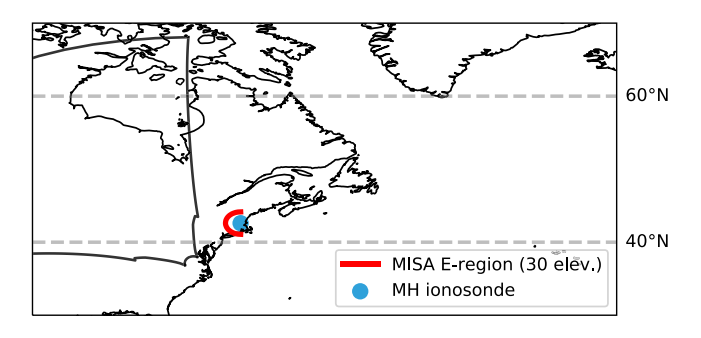


Figure 1. A map showing the field-of-view of the BKS SuperDARN radar as a black outline along with the location of the Millstone Hill ionosonde as a blue dot. In addition, the potential area covered by the Millstone Hill ISR's MISA antenna at 30° elevation and 200 km range is marked by the red arc.

scale size of sporadic E layers (a few hundred kilometers), it is reasonable to associate the effects observed by the MISA and BKS radars. However, any structure in the layer on scales smaller than the separation would tend to decorrelate the observations.

2.3. Millstone Hill Ionosonde

We will use ionograms provided by the Global Ionospheric Radio Observatory (GIRO) (Galkin et al., 2018; Reinisch & Galkin, 2011) to analyze the characteristics of Es layers. In particular, we will examine two standard URSI characteristics of Es provided automatically by ionogram autoscaling software (e.g., Galkin et al., 2018; Pezzopane et al., 2010), its critical frequency (foEs) and the minimum virtual height (h'Es) to determine the relationship between Es and tidal motion provided by the Millstone Hill ISR. GIRO ionosondes installed at more than 120 locations across the world have contributed their measurements to the GIRO portal at http://giro.uml.edu. In this study,

we will analyze ionograms recorded by the Millstone Hill Digisonde DPS-4D. Extracted ionogram traces are inverted to obtain the bottomside vertical electron density profile at the observatory location. Echo traces corresponding to the sporadic E layer are not routinely inverted; however, due to the typically low thickness of the Es layer that do not exceed 2 km and low density of the underlying plasma below Es, the h'Es values are close to the true heights (hEs). The interpretation of Millstone Hill ionograms is usually performed using a tool called Automatic Real-Time Ionogram Scaler with True height (ARTIST) version 5 (Galkin et al., 2008). Figure 2 shows two examples of autoscaled ionograms that were recorded on 3 June 2022 at 16 UT (left panel) and 22 UT (right panel), during the experimental campaign between the BKS SuperDARN and Millstone Hill. The horizontal axis shows the frequencies of the transmitted radio signals and the vertical axis shows the virtual heights of ionospheric layers. The critical frequencies and heights of the E and F layers of the ionosphere are summarized on the left-side of each panel. Both ionograms indicate the presence of Es during the campaign with foEs reaching 4.3 MHz (left)/5.28 MHz (right), and hEs is identified as 102.5 km (left)/115 km (right). The ionograms used in our analysis were manually inspected and scaled appropriately where needed.

3. Observations

In this section, we analyze and compare the observations made by the Millstone Hill ionosonde, MISA, and the BKS SuperDARN radar during the experiment on 3–4 June 2022. The experiment started after MISA began operations at 1300 UT and ended at 0400 UT. The entire interval was geomagnetically quite with a maximum Kp index of 1.

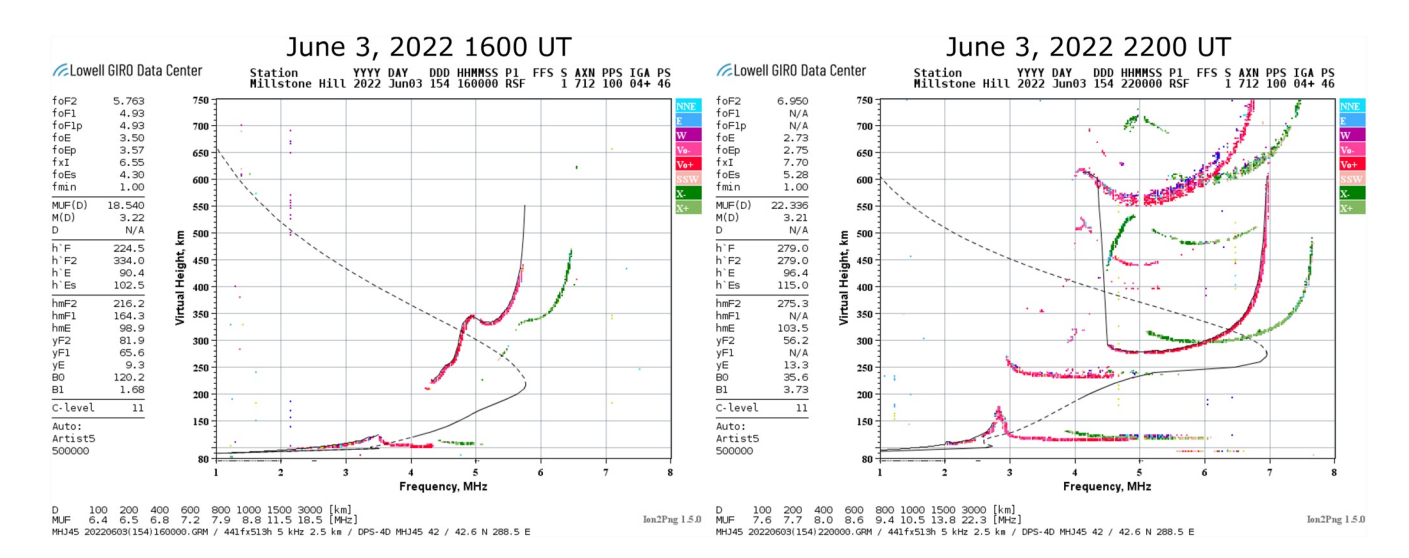


Figure 2. Ionograms describing the state of the bottom-side ionosphere near the Millstone Hill observatory at 16 UT (left) and 22 UT (right) on 3 June 2022. Both ionograms clearly show the presence of Es layers with critical frequencies reaching 4.3 MHz (left) and 5.28 MHz (right).

KUNDURI ET AL. 4 of 14

21699402, 2023, 9, Downloaded from https://agupubs.onlinelibrary.wiley.com/doi/10.1029/2023JA031455, Wiley Online Library on [11/07/2024]. See the Terms and Conditional Condi

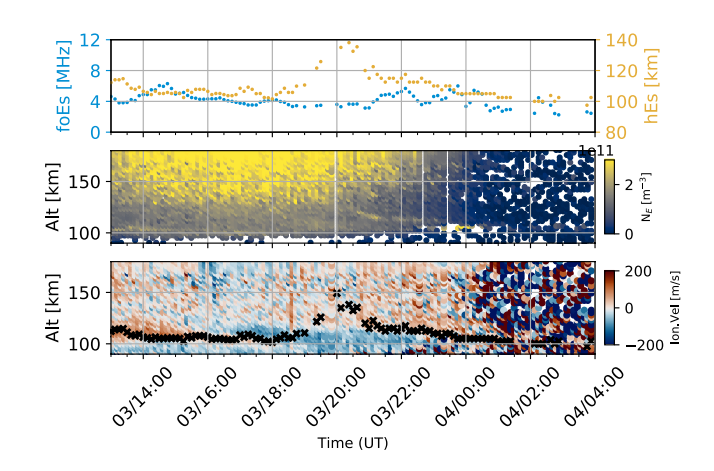


Figure 3. Time series plot showing observations by the Millstone Hill ISR's MISA antenna and the Millstone Hill ionosonde on 3–4 June 2022. The top panel shows the critical frequency and the height of the Es layer observed by the ionosonde. The middle and bottom panels show electron densities and line-of-sight ion velocities measured by MISA; "x" indicates the height of the Es (hEs) layer measured by the ionosonde.

We begin with the observations from the MISA antenna and the Millstone Hill ionosonde on 3-4 June 2022 between 1300 and 0400 UT shown in Figure 3. The top panel shows a time-series plot of hEs and foEs determined from the ionosonde, while the middle and the bottom panels show electron densities and ion velocities measured by MISA, respectively. hEs measured by the Millstone Hill ionosonde is also overlaid on bottom panel for reference. Ionosonde observations during the event reveal the presence of an Es layer consistently throughout the entire interval. The Es layer during the earlier phase of the event (between 13 and 20 UT) at altitudes ~100 km was not observed in MISA estimated electron densities. Since the Es layer was located at the lower extent of altitudes where MISA was making measurements, the clutter reduction algorithms employed at these close ranges might have suppressed the Es observations. It is also possible that the altitudinal resolution of MISA (1.3 km) during the experiment was not sufficient to resolve the Es layer. However, after 21 UT a clear Es layer does appear in MISA observations at altitudes close to 130-140 km hE derived from the ionosonde closely tracks the motion of the Es layer during this phase. The bottom panel shows LoS ion velocities measured by MISA, which reached ~100 m/s in magnitude. A comparison between hEs and ion velocities in the bottom panel brings out two important features: (a) the ion velocities indicate a clear semidiurnal tidal structure, and (b) hEs follows the tidal pattern

observed by MISA. The relationship between hEs and the tidal pattern observed by MISA will become more evident in the next sections where we will further explore the correlation between hEs and wind shears.

In Figure 4, we compare the tidal structure observed in MISA ion velocities with predictions from the Horizonal Wind Model (HWM-14) (Drob et al., 2015). It is noteworthy that ion velocities at lower altitudes (below ~110–120 km) can be used as direct tracers of neutral winds (Evans, 1972a, 1972b, 1978). This comparison therefore provides an opportunity to analyze MISA observations against a baseline (HWM-14 estimates). The first and second panels in the figure show the zonal and meridional components of neutral winds estimated by HWM-14 as a function of altitude and time. The third panel shows the resultant HWM-14 winds projected along the MISA look direction, and the bottom panel shows the actual LoS winds measured by MISA. MISA and HWM-14 LoS vectors both show a semidiurnal tidal structure and are qualitatively consistent below 120–130 km. MISA velocities are, however, stronger in magnitude, reaching ~100 m/s as compared to HWM-14 LOS velocities which maximize at ~50 m/s. Overall, however, the HWM-14 model morphology appears to be in agreement with the observations near Millstone Hill in a qualitative sense during a geomagnetically quiet day.

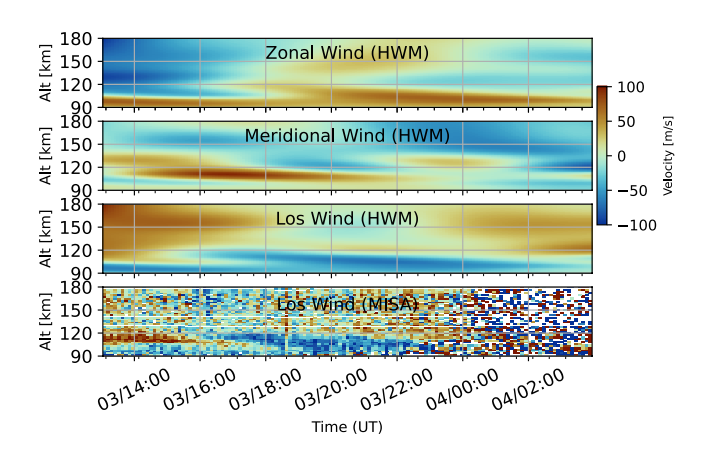


Figure 4. Time series plot showing a comparison between the estimates of neutral winds from the Horizontal Wind Model 14 (HWM-14) and MISA observations. The first two panels show zonal and meridional winds from HWM-14. The third panel shows the HWM-14 wind estimates projected along the direction of MISA. The last panel shows ion velocities observed by MISA.

Observations presented in Figure 4 showed that HWM-14 estimates and MISA LOS velocities showed similar behavior and exhibited semidiurnal tidal structures. We therefore continue by assuming that HWM-14 provides a reliable estimate of the direction of the neutral winds, and use this component information to resolve MISA LOS vectors into zonal and meridional directions. The LoS velocities measured by MISA (V_{LOS}) can be expressed in terms of meridional and zonal components as: $V_{LOS} = V_{North} \cos(\theta_{LOS}) + V_{East}$ $\sin(\theta_{LOS}),$ where θ_{LOS} is the azimuth MISA was pointing toward, V_{North} is the northward velocity, and $V_{\textit{East}}$ is the eastward velocity. As noted in Section 2.2, θ_{LOS} during our experiment was -120° . Consequently, V_{North} is projected along the LoS by a factor of $\cos(-120^{\circ})$ or -0.5, and V_{East} by a factor of $\sin(-120^{\circ})$ or -0.86. In other words, if the radar were measuring purely zonal flows, V_{LOS} would have a sign opposite to the V_{East} and a magnitude ~86% of V_{East} . Similarly, if the radar were measuring purely meridional flows, V_{LOS} would have a sign opposite to the V_{North} and a magnitude that is 50% of V_{North} . While θ_{LOS} tends to favor zonal flows by a small factor, MISA can still measure contributions from meridional flows. For example, in Figure 4, between 16 and 18 UT and just below 120 km, we can note that the HWM zonal winds are negative (top panel), meridional winds are positive (second panel), and

KUNDURI ET AL. 5 of 14

21699402, 2023, 9, Downloaded from https://agupubs.onlinelibrary.wiley.com/doi/10.1029/2023JA031455, Wiley Online Library on [11/07/2024]. See the Terms

and-conditions) on Wiley Online Library for rules of use; OA articles are governed by the applicable Creative Commons License

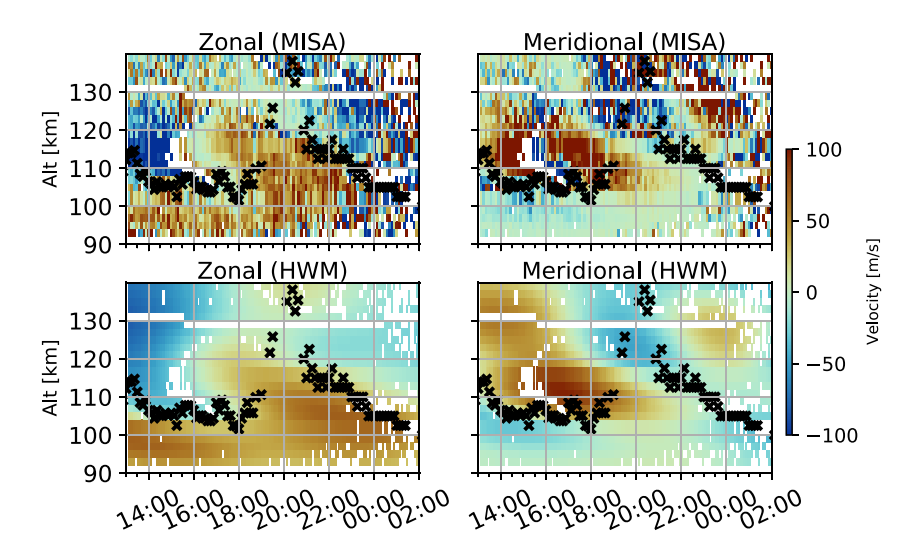


Figure 5. A comparison between zonal (left) and meridional (right) velocities by MISA (top) and HWM-14 (bottom). Line-of-sight MISA observations are resolved into zonal and meridional components using the directionality estimates provided by HWM-14 model. 'x' indicates the height of the Es (hEs) layer measured by the ionosonde. See text for details.

projection of HWM along LOS (third panel from top) shows negative velocities. This suggests that stronger meridional winds are contributing to the LOS, which are opposite in sign to the meridional winds. Figure 5 shows a comparison between MISA LOS velocities (top panels) and HWM-14 estimates (bottom panels) resolved into zonal (left) and meridional (right) directions. We note that the zonal components of both MISA and HWM-14 show a tidal structure switching between eastward (positive) and westward (negative) directions. The meridional components exhibit a similar behavior and alternate between southward and northward directions. More importantly, we note that hEs (indicated by "x") is located in regions where zonal winds transition from eastward to westward orientation, notably between 13 and 18 UT and 21 and 2 UT. For the meridional component, hEs is located in the region where winds are turning from a southward to a northward orientation between 13 and 18 UT. For the interval between 21 and 2 UT, hEs is located in a region where northward winds are turning into a narrow region of southward winds and then subsequently turning back to northward orientation at higher altitudes.

We further analyze the relation between the zonal and meridional components of the winds and hEs in Figure 6 which is in the same format as Figure 5 but indicates vertical gradients in the velocities. The figure shows that hEs is located in regions with strong negative zonal shear between 13 to 18 UT and 21 to 2 UT. On the other

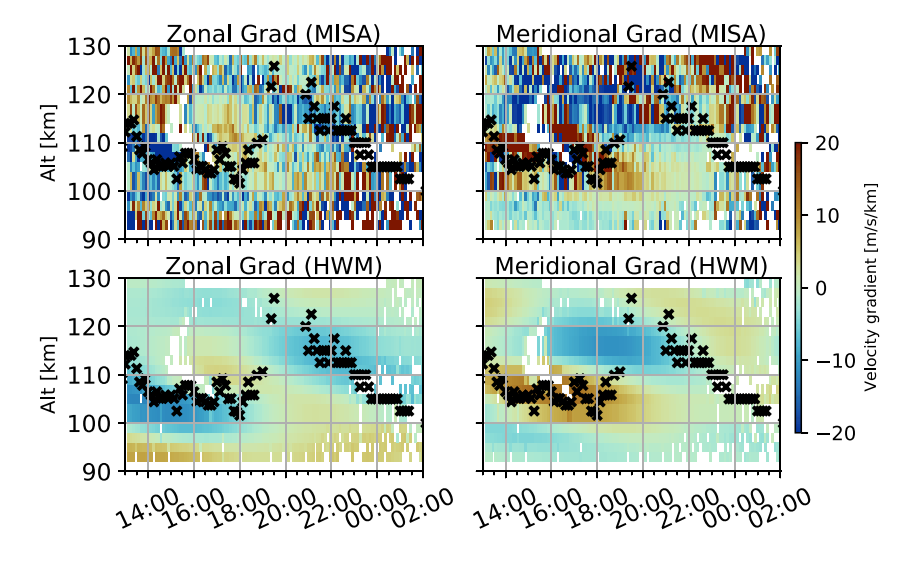


Figure 6. Same format as Figure 5 but for velocity gradients.

KUNDURI ET AL. 6 of 14

21699402, 2023, 9, Downloaded from https://agupubs.onlinelibrary.wiley.com/doi/10.1029/2023JA031455, Wiley Online Library on [11/07/2024]. See the Terms and Conditions (https://onlinelibrary.wiley.com/terms

and-conditions) on Wiley Online Library for rules of use; OA articles are governed by the applicable Creative Commons License

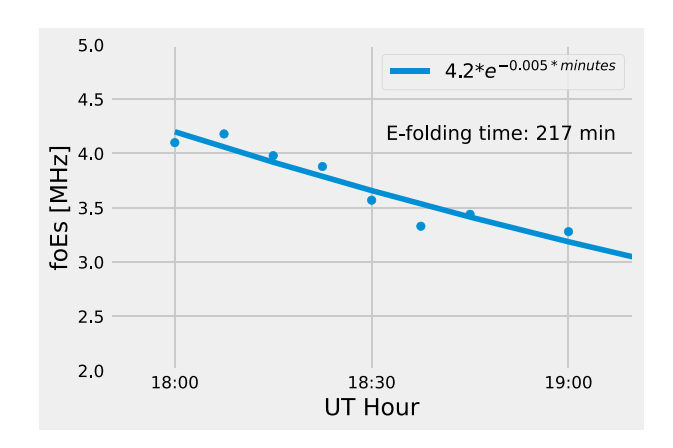


Figure 7. Time scales associated with Es delayering in the absence of wind shears between 18 and 19 UT. Blue dots represent foEs observed by the Millstone Hill ionosonde and the blue curve is the best fit exponential curves for the data points.

hand, we find that hEs is located at altitudes with a positive meridional shear between 13 and 18 UT. While hEs is located in a region with positive meridional gradients between 21 and 2 UT, the shears are not as strong compared to observations between 13 and 18 UT. We further note that the zonal shears are turned off after 18 UT, and hEs appear to increase between 18 and 19 UT. After 1930 UT, hEs reappears at higher altitudes, following another change in the tidal pattern. We use the ion temperatures measured by MISA, along with estimates of neutral temperature and densities provided by the Naval Research Laboratory Mass Spectrometer Incoherent Scatter radar (NRLMSIS) model (Emmert et al., 2021), to estimate ion-neutral collision frequencies and thereby vertical ion speeds through Equation 1. The equations for ion-neutral collision frequencies summarized in Schunk and Nagy (2009) are used, and the value of ion gyrofrequency is taken from Didebulidze et al. (2020). Our calculations show that ν/ω_i exceeds a value of 1 near 130 km, suggesting that zonal winds can dominate at altitudes lower than 130 km. The methodology is summarized in the supplementary material. The behavior of Es layers in the absence of wind shears is further analyzed in Figure 7 which shows a time series plot of foEs (indicated by blue dots) between 18 and 19 UT when the negative zonal wind shears were turned off. An exponential fit to the data

points is marked in Figure 7 as a blue line and the e-folding time estimated from the fit is 217 min. In the next section we will further examine the relationship between hEs and the zonal/meridional components of the winds and compare our observations with previous studies.

So far, we have presented observations made by Millstone Hill ISR's MISA antenna and the ionosonde. In Figure 8, we present the power measured during a full scan by the BKS radar on 2 May 2022 (left) and 3 June 2022 (right) at 16 UT. The first scan was chosen during summer when there were no reports of Es from the Millstone Hill and Wallops ionosondes. The second scan on 3 June 2022 occurred during the experimental campaign when Es were observed. It can be noted that the radar was operating at the same frequency of 11.5 MHz during both the scans. Both panels show 1-hop ground scatter and the differences in the location of the backscatter observed are clearly evident. Namely, in the absence of Es, the ground backscatter is observed at farther ranges, and in the presence of Es, the backscatter moves to closer ranges. The differences in SuperDARN backscatter during Es and non E days become more evident in Figure 9 which shows range time plots during non Es (top panel) and E days (middle and bottom panels) from beam 22 of the BKS radar and beam 21 of the Fort Hays East (FHE) Radar. We can clearly note from the top and middle panels that in the absence of Es, ground backscatter is observed by the BKS radar between 1,000 and 1,500 km. On the other hand, in the presence of Es, BKS ground scatter moves

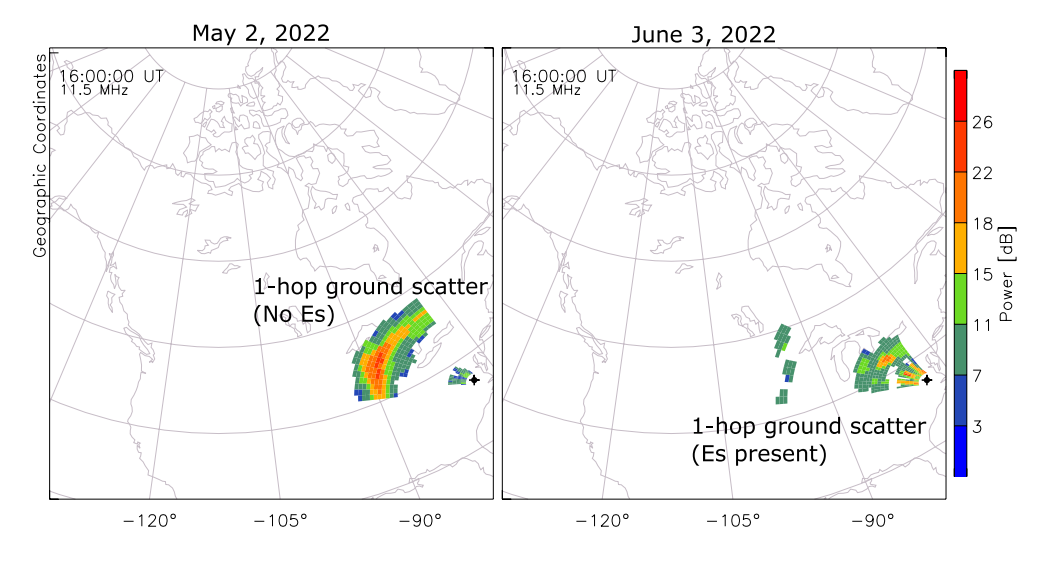


Figure 8. BKS radar observations of the backscatter power measured during a full scan beginning at 16 UT on 2 May 2022 (left) and 3 June 2022 (right).

KUNDURI ET AL. 7 of 14

21699402, 2023. 9, Downloaded from https://agupubs.onlinelibrary.wiley.com/doi/10.1029/2023JA031455, Wiley Online Library on [11/07/2024]. See the Terms and Conditions (https://on

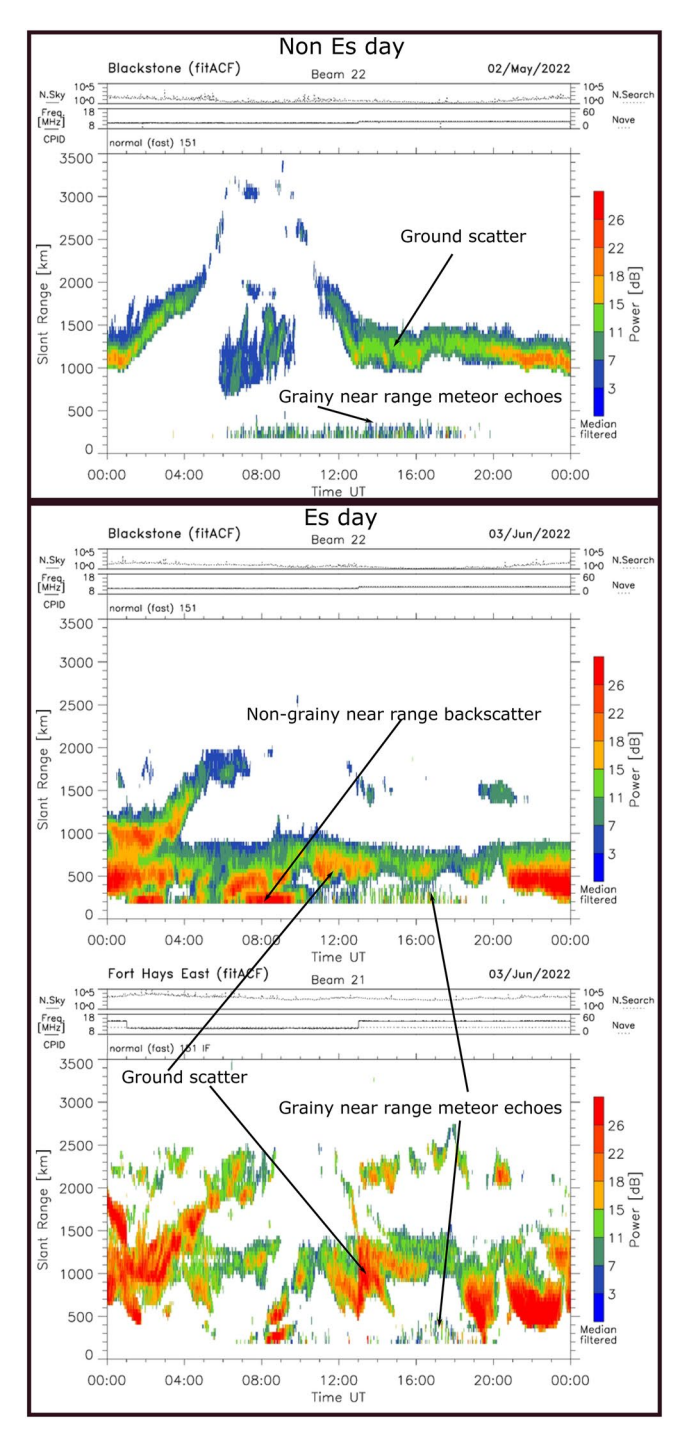


Figure 9. A range versus Universal Time (UT) plot showing backscattered power measured during non Es (2 May 2022) and E days (3 June 2022). The top panel shows measurements along beam-22 of the BKS radar during the non E day. The middle and bottom panels show measurements along beam-22 of the BKS radar and beam-21 of the Fort Hays East (FHE) radar respectively, during the Es days. Categories of backscatter discussed in the text are labeled.

closer to the radar and is observed between 500 and 1,000 km. Another important feature is the notable change in near-range BKS backscatter (in the first 7 range gates) on the day E was reported. Specifically, we can observe that all three panels show the presence of near range grainy echoes between 0600 and 1800 UT, which are typically associated with meteors (Chisham & Freeman, 2013; Hall et al., 1997). However, a closer examination of the middle panel shows extended intervals of non-grainy near range BKS backscatter between 0100 and 1000 UT with backscatter power exceeding 30 dB. This non-grainy backscatter is observed only by the BKS radar and not by the FHE radar (bottom panel). We will further analyze the relation between Es occurrence and near range backscatter observed by SuperDARN in Section 4.

The impact of Es on SuperDARN ground scatter is further examined using numerical ray-tracing analysis in Figure 10. In this study, we use the ray-tracing model developed by de Larquier et al. (2013) which relies on a two-dimensional formulation of Fermat's principle in the propagation plane Coleman (1998). Specifically, BKS radar operations are simulated along beam-22 at an operational frequency of 11 MHz. Similar to previous approaches and representative of typical SuperDARN operations (de Larquier et al., 2011, 2013), rays are launched at all elevation angles between 5° and 55° in steps of 0.1°, at the selected azimuth and frequency. We use the 2016 version of the International Reference Ionosphere (IRI-2016) (Bilitza et al., 2017) and the thirteenth generation of the International Geomagnetic Reference Field (IGRF-13) (Alken et al., 2021) with the ray tracing model. The electron densities are color-coded according to the color bar on the right. Rays are plotted in magenta and the black shaded segments along the ray paths mark regions with good aspect conditions (within 1° of orthogonality to background magnetic field) where it is possible for the radar to observe 1/2 hop ionospheric backscatter. Rays that are reflected to the ground are identified as 1 hop ground scatter. The top panel shows a ray-tracing simulation in the default IRI ionosphere, and we can notice a band of ground scatter centered near 1,000 km. An artificial Es layer with electron densities of 6×10^{11} m⁻³ (foEs = 7 MHz) at 97 km altitude and 2×10^{11} m⁻³ (foEs = 4 MHz) at 122 km altitude are included in the middle and the bottom panels, respectively. The Es layers are included in the first 500 km range. It can be clearly noted that Es layers act as strong reflectors and SuperDARN ground scatter moves to closer ranges due to reflections from these layers, similar to the observations presented in Figures 8 and 9. The ray-tracing approach in Figure 10 uses IRI-2016 with an artificial Es layer. While these simulations suggest SuperDARN ground scatter location and power can potentially be used to remotely sense Es layers, the ionosphere in reality can be more complex producing noticeable variability in SuperDARN backscatter. For example, Es and intermediate layers can be associated with disturbances such as gravity waves (Earle et al., 2000; Roddy et al., 2007), which are known to produce quasi-periodic enhancements in SuperDARN power (Bristow et al., 1994). A more rigorous approach can therefore include using data from the ionosondes (e.g., those located at mid-latitudes-Wallops Island or Millstone Hill) to scale and modify the background ionosphere in ray-tracing, and quantify the variability and uncertainties in SuperDARN backscatter in the presence of Es. We will analyze the impact of Es on SuperDARN observations in the next section.

4. Discussion

In the previous section, the characteristics of Es observed in the Millstone Hill ionosonde data were compared with MISA observations of ion velocities

KUNDURI ET AL. 8 of 14

21699402, 2023. 9, Downloaded from https://agupubs.onlinelibrary.wiley.com/doi/10.1029/2023JA031455, Wiley Online Library on [11/07/2024]. See the Terms and Conditions (https://on

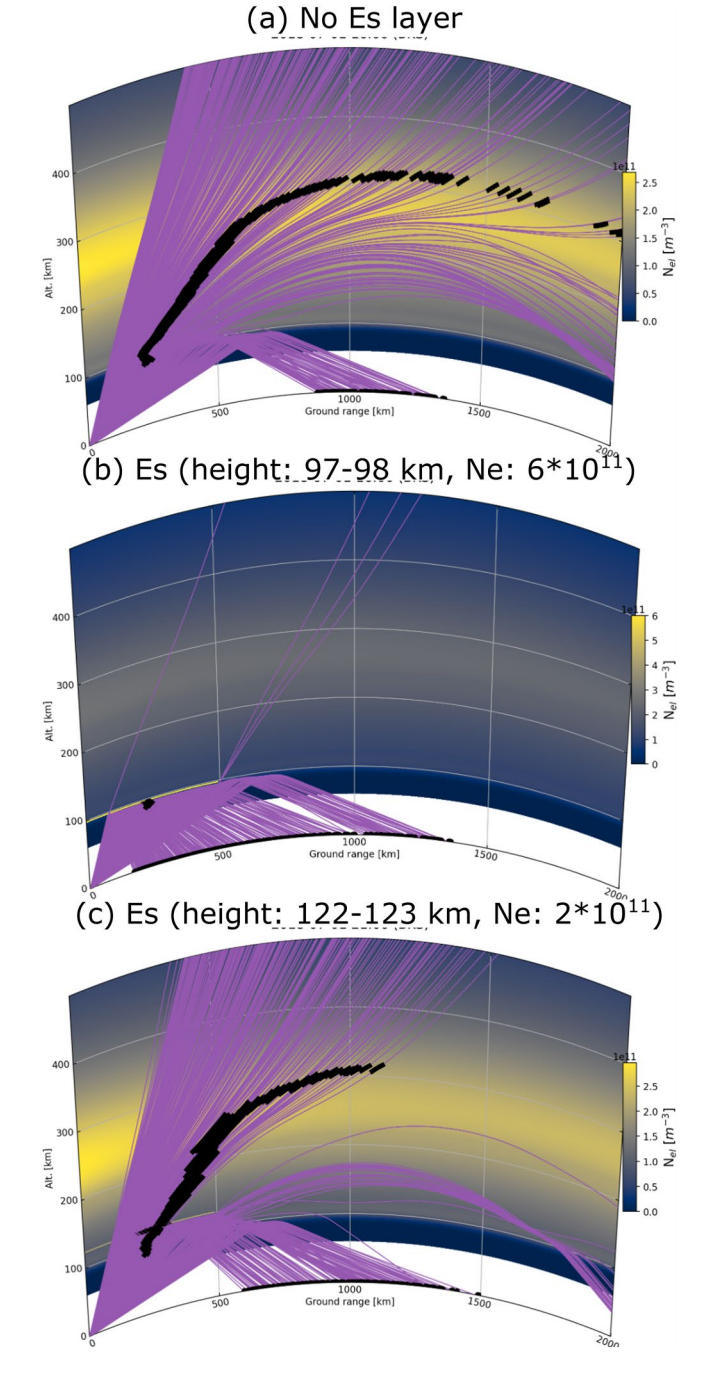


Figure 10. Ray-tracing results in an International Reference Ionosphere (IRI) generated ionosphere for beam 22 of the BKS radar on 3 June 2022 at 16:00 UT. (a) ray-tracing without any Es layer, (b) Es layer manually inserted between 97 and 98 km altitude with an electron density of 6×10^{11} m⁻³, (c) Es layer manually inserted between 122 and 123 km altitude with an electron density of 2×10^{11} m⁻³. Each ray is plotted in magenta and the length of a ray path to a scatter point is the slant range. Black segments mark regions where rays are within one degree of orthogonality with the background geomagnetic field lines and provide the aspect conditions suitable for observing ionospheric backscatter. See text for details.

in the E-region. In addition, the impact of Es on HF propagation was examined using observations from the BKS SuperDARN radar and ray-tracing analysis. Here, these observations will be compared with those presented in previous studies, and the role of different factors in generating Es will be discussed.

The wind-shear theory has been considered by several previous studies as the primary mechanism generating Es layers (Axford, 1963; Haldoupis, 2011; Shinagawa et al., 2021; Whitehead, 1961). However, a few studies have reported observations inconsistent with wind-shear theory. For example, Hall et al. (1971) presented rocket observations of Es when the gradients in vertical ion speed were positive (i.e., $\nabla w_i > 0$ in Equation 1), contrary to the negative gradients hypothesized by the wind-shear theory. Similarly, Liu et al. (2018) found a weak correspondence between wind shears estimated from the Thermosphere Ionosphere Mesosphere Energetics and Dynamics (TIMED) satellite and Es observations derived from radio occultation measurements. Figures 3, 5 and 6, in this study indicate that hEs derived from the Millstone Hill ionosonde data varies systematically with the tidal motion and Es is located in a region with strong vertical shears in the winds, consistent with the wind shear theory, except for the interval between ~18 and 19 UT. During this period we find only a weak correspondence between wind-shears (especially zonal) and hEs and the observations are no longer consistent with the wind shear theory. However, it is likely that Es observations during this interval are decaying layers surviving after the wind shears are turned off. It is therefore plausible that some of the previous reports of Es that were inconsistent with the wind-shear theory were likewise decaying layers surviving after the shears were turned off. In fact, we can find from Figure 7 that foEs decreases during this interval (between 18 and 19 UT) with an e-folding time of \sim 3.5 hr. This \sim 3.5 hr e-folding time is longer than the \sim 1–2 hr ion convergence time estimated previously using the International Reference Ionosphere and the Mass Spectrometer and Incoherent Scatter models (Bishop & Earle, 2003; Haldoupis, 2011). This inconsistency could be due to incomplete atmospheric chemistry used to drive the models. Diffusion is another factor that would also play an important role in the decay of Es layers, especially at higher altitudes. More observations are necessary to further investigate this inconsistency between theoretical estimates and observations.

Figures 3, 5 and 6 also indicate that hEs derived from the Millstone Hill ionosonde data varies systematically with the tidal motion traced by the ion velocities measured by MISA (and also the HWM-14 model estimates). In particular, our observations are consistent with previous studies (e.g., Wilkinson et al., 1992; Haldoupis et al., 2004; Christakis et al., 2009; Arras et al., 2009) which suggested that the diurnal and semidiurnal atmospheric tides play an important role in the formation of Es layers. Tidal signatures were often observed as a downward motion in Es layers (e.g., Haldoupis et al., 2006). Our observations in Figure 5 clearly indicate a similar descent in Es layers between 1300-1800 UT and 2000-0130 UT, closely following the tidal motion. This correlation between hEs and tides is not unexpected since the dominant winds in the region are the solar tides during geomagnetically quiet conditions, and they are expected to be an important source of vertical shears in the neutral wind at mid-latitudes (Haldoupis, 2012; Lindzen & Chapman, 1969). Observations of electron densities from the Arecibo ISR were analyzed by Christakis et al. (2009) and the authors showed that the diurnal tide controls the formation and descent of Es at altitudes below 110 km, and the semidiurnal tide is dominant at higher altitudes.

KUNDURI ET AL. 9 of 14

However, our observations in Figures 3 and 5 do not reveal a dominant diurnal tide and are thus not consistent with Christakis et al. (2009). One explanation for this discrepancy could be that diurnal tides are expected to have higher amplitudes at lower latitudes (where Arecibo observations were made), and lower amplitudes at mid-latitudes (where our observations were made) (e.g., Davis et al., 2013). While Christakis et al. (2009) used over 100 days of observations in their analysis to show a dominant tidal component, our analysis was limited to observations spanning 1 day. However, it is noteworthy that previous studies (e.g., Goncharenko & Salah, 1998; Wand, 1983) used measurements from the ISR at Millstone Hill to examine the climatology of neutral winds in the lower thermosphere. Both showed strong and dominant semidiurnal winds. Overall, our observations and these previous statistical results from Millstone Hill ISR suggest that the semidiurnal component is dominant at mid-latitudes. However, a more comprehensive set of experiments directly comparing Millstone Hill ISR measurements with observations of Es will be useful in fully determining the role of diurnal and semidiurnal components in generating Es at mid-latitudes.

The relative contributions of vertical shears in zonal (U) and meridional (V) winds in generating Es layers have also been a topic of active research. From Equation 1, we can note that Es layers form during vertical ion convergence $(\frac{\partial w_i}{\partial z} < 0)$ and this can happen when there are strong negative gradients in zonal winds and/or strong positive gradients in meridional winds. Moreover, it is evident that $\frac{v_i}{\omega_i}$ plays an important role in determining the contributions of U and V. At lower altitudes below 115–120 km, it is usually expected that $\frac{v_i}{\omega_i} \gg 1$ (Arras et al., 2009; Bishop & Earle, 2003; Haldoupis, 2012) and so, zonal wind shears are expected to dominate at these altitudes. However, Krall et al. (2020) used numerical simulations to suggest that meridional winds were the dominant drivers at altitudes below 110 km at Arecibo, in contrast to studies that reported the dominance of zonal winds (e.g., Carter & Forbes, 1999; Yamazaki et al., 2022). Our simulated observations in Figure 5 show that Es between 13 and 18 UT is observed in a region characterized by a westward (negative) wind above and an eastward (positive) wind below, where vertical shears in zonal wind are negative (see Figure 6). Observations from Figure 6 suggest that the Es layers are also collocated with positive gradients in meridional winds between 13 and 18 UT. However, a closer examination of Figure 6 shows that Es layers stop following the tidal motion ~18 UT, after the zonal shears are turned off, even though the meridional gradients continue to exist until ~20 UT. These observations suggest that while meridional winds can play some role in generating and controlling Es, the zonal wind component is dominant at lower altitudes, consistent with the observations presented by Earle et al. (2000); Carter and Forbes (1999); Yamazaki et al. (2022). The inconsistency with the Krall et al. (2020) simulations could be attributed to the fact that Arecibo is located at lower latitudes than Millstone Hill and the neutral dynamics could be different in these two locations. At higher altitudes, above 130 km, both zonal and meridional winds are expected to equally contribute to the generation of Es (Christakis et al., 2009). During our experimental campaign, the peak height Es reached was ~140 km, near 21 UT. From Figures 5 and 6, Es layers observed after 21 UT were collocated with negative gradients in zonal winds (albeit weaker than those observed between 13 and 18 UT) and positive gradients in meridional winds. It is possible that both components are equally dominant during this interval. However, more observations are required to fully resolve the relative contributions of zonal and meridional components at higher altitudes near Millstone Hill.

An important fact that contributes to the formation of Es is meteor influx which supplies the metallic ions that constitute these layers. This relationship between Es and meteors has only been validated indirectly using (1) separate non-collocated measurements of Es (e.g., ionosondes) and meteor influx (e.g., meteor radars (Haldoupis et al., 2007) or (2) via models (Feng et al., 2013). One advantage with our experimental campaign is that grainy near range SuperDARN backscatter can provide an estimate of meteor influx (Hall et al., 1997), which can help elucidate the relationship between Es and meteors. A comparison between SuperDARN observations during non Es and Es days shown in Figure 9 reveals no significant increase in the grainy near range echoes in both BKS and FHE radar data during the Es day. However, on the Es day, the BKS radar observes localized non-grainy near range backscatter in the same ranges where grainy meteor echoes are typically observed (Chisham & Freeman, 2013). Taken together, the non-grainy structure of this backscatter, and the fact that it is only observed by the BKS radar (and not by the FHE radar) over a limited geographical region, raises the possibility that it is not of meteoric origin. Previous studies have shown that mid-latitude Es can be highly structured and "patchy" (e.g., Miller & Smith, 1975; Yamamoto et al., 1992), and such "patchy" Es layers can drive plasma instabilities, producing plasma density irregularities (Hysell et al., 2002, 2009, 2014; Yamamoto et al., 1992). It is possible that some of the non-grainy near range BKS observations might be direct backscatter from Es layers. Our

KUNDURI ET AL. 10 of 14

21699402, 2023, 9, Downloaded from https://agupubs.onlinelibrary.wiley.com/doi/10.1029/2023JA031455, Wiley Online Library on [11/07/2024]. See the Terms and Conditions

onditions) on Wiley Online Library for rules of use; OA articles are governed by the applicable Creative Commons Licenso

previous study (Kunduri et al., 2022) showed that the E-region backscatter and meteor scatter can occur in the same ranges and such backscatter increases during summer, when Es are most frequently observed. Identifying the source of the non-grainy echoes is beyond the scope of our current analysis, but will be pursued during future experimental campaigns between the Millstone Hill ISR and SuperDARN. Observations from the FHE and BKS radar in Figure 9 show no significant increase in grainy meteor scatter during the E day. This suggests an increase in meteoric deposition rate might not be the dominant source of the metallic ions constituting the Es layers. It is possible that the formation of Es on this day could be associated with the meridional transport of ions caused by the winter-to-summer lower thermospheric circulation driven by gravity wave forcing (Hodos et al., 2022; Yu et al., 2021).

Our analysis also provides an opportunity to determine the impact of Es on HF propagation. Two features can be observed from Figures 8-10: (a) Es enables short range communications, with rays at higher elevation angle reaching closer ranges, and (b) both foEs and hEs have an impact on HF rays such that, higher foEs and lower hEs cause HF rays to reach shorter ranges. Our observations are thus consistent with the results presented in Cameron et al. (2022) who showed that HF transmissions in Qaanaaq, Greenland were received in Alert, Canada. The authors used ray-tracing to show that the prolonged and consistent observations of frequencies reaching 14.4 MHz with a uniform and high signal-to-noise ratio were consistent with reflection from Es layers at ~ 100 km.

In summary, our experimental campaign provided an excellent opportunity to analyze nearly-collocated and simultaneous measurements of meteor deposition rate, atmospheric tides, and Es over extended intervals of time. Our results suggest that Es generation, especially during geomagnetically quiet intervals, is strongly influenced by atmospheric tides consistent with the wind-shear theory. Finally, reflections from Es are shown to produce a significant change in HF ground backscatter.

5. Conclusions

In this paper, we present results from a coordinated experimental campaign between the Millstone Hill ISR, BKS SuperDARN radar, and the Millstone Hill ionosonde on 3–4 June 2022. The primary goal of this experiment was to examine the dynamics of Es layers continuously over extended intervals of time, and to determine the role of different factors such as atmospheric tides and meteor influx in Es generation. We find that Es layers are predominantly observed in regions with strong vertical wind-shears, consistent with the wind-shear theory. Furthermore, we observe that zonal wind-shears are more important (when compared to meridional wind shears) for the generation of Es at altitudes below 110 km. Observations by the BKS SuperDARN radar indicate an increase in the number of meteor echoes when Es is observed, suggesting that metallic ions from meteors could in fact be seeding the Es layers and accounting for the well known maximum in Es occurrence. Overall, our results suggest that over large spatial scales Es can exhibit at times a deterministic rather than a random or sporadic process, whose occurrence is predominantly governed by the permanent global system of thermally driven tides and meteor deposition rate. Observations from the BKS SuperDARN radar indicate that reflections from Es can significantly alter HF propagation and communication systems. In a future study, we will explore a methodology to use mid-latitude SuperDARN as a tool to monitor Es over large geographical regions.

Data Availability Statement

Millstone Hill ISR data used in this study can be accessed from Madrigalweb (https://w3id.org/cedar?experiment_list=experiments/2022/mlh/03jun22&file_list=mlh220603g.003.hdf5). SuperDARN data during the interval analyzed in this study can be accessed from https://doi.org/10.5281/zenodo.8209766. Millstone Hill digisonde data during the interval can be accessed from https://doi.org/10.5281/zenodo.8209770. Kp index has been accessed from WDC Kyoto https://wdc.kugi.kyoto-u.ac.jp/kp/index.html. We also acknowledge the use of pyDARN version 3.1.1 (https://zenodo.org/record/7767590) in plotting and reading SuperDARN data.

References

Alken, P., Thébault, E., Beggan, C. D., Amit, H., Aubert, J., Baerenzung, J., et al. (2021). International geomagnetic reference field: The thirteenth generation. *Earth Planets and Space*, 73(1), 1–25. https://doi.org/10.1186/s40623-020-01281-4

Arras, C., Jacobi, C., & Wickert, J. (2009). Semidiurnal tidal signature in sporadic e occurrence rates derived from gps radio occultation measure-

ments at higher midlatitudes. Annales Geophysicae, 27(6), 2555–2563. https://doi.org/10.5194/angeo-27-2555-2009

Acknowledgments

We thank the National Science Foundation for support under Grants AGS-1839509, AGS-1935110, and AGS-1952737 and NASA for support under Grant 80NSSC22K1635. This work acknowledges support by the NASA DRIVE Science Center for Geospace Storms (CGS) under award 80NSSC22M0163. Observations and analysis at the Millstone Hill Geospace Facility are supported by NSF grant AGS-1952737 to the Massachusetts Institute of Technology. The Blackstone SuperDARN radar is maintained and operated by Virginia Tech under the support of NSF Grant AGS-1935110.

KUNDURI ET AL. 11 of 14

21699402, 2023, 9, Downloaded from

- Arras, C., & Wickert, J. (2018). Estimation of ionospheric sporadic e intensities from gps radio occultation measurements. *Journal of Atmospheric and Solar-Terrestrial Physics*, 171, 60–63. https://doi.org/10.1016/j.jastp.2017.08.006
- Arras, C., Wickert, J., Beyerle, G., Heise, S., Schmidt, T., & Jacobi, C. (2008). A global climatology of ionospheric irregularities derived from gps radio occultation. *Geophysical Research Letters*, 35(14), L14809. https://doi.org/10.1029/2008GL034158
- Axford, W. I. (1963). The formation and vertical movement of dense ionized layers in the ionosphere due to neutral wind shears. *Journal of Geophysical Research* (1896-1977), 68(3), 769–779. https://doi.org/10.1029/JZ068i003p00769
- Bilitza, D., Altadill, D., Truhlik, V., Shubin, V., Galkin, I., Reinisch, B., & Huang, X. (2017). International reference ionosphere 2016: From ionospheric climate to real-time weather predictions. Space Weather, 15(2), 418–429. https://doi.org/10.1002/2016SW001593
- Bishop, R. L., & Earle, G. D. (2003). Metallic ion transport associated with midlatitude intermediate layer development. *Journal of Geophysical Research*, 108(A1), 1019. SIA 3–1–SIA 3–8. https://doi.org/10.1029/2002JA009411
- Bristow, W. A., Greenwald, R. A., & Samson, J. C. (1994). Identification of high-latitude acoustic gravity wave sources using the goose bay hf radar. *Journal of Geophysical Research*, 99(A1), 319–331. https://doi.org/10.1029/93JA01470
- Cameron, T., Fiori, R., Themens, D., Warrington, E., Thayaparan, T., & Galeschuk, D. (2022). Evaluation of the effect of sporadic-e on high frequency radio wave propagation in the arctic. *Journal of Atmospheric and Solar-Terrestrial Physics*, 228(105), 826. https://doi.org/10.1016/j.jastp.2022.105826
- Carmona, R. A., Nava, O. A., Dao, E. V., & Emmons, D. J. (2022). A comparison of sporadic-e occurrence rates using gps radio occultation and ionosonde measurements. *Remote Sensing*, 14(3), 581. https://doi.org/10.3390/rs14030581
- Carter, L., & Forbes, J. (1999). Global transport and localized layering of metallic ions in the upper atmosphere. Annales Geophysicae, 17, 190–209. https://doi.org/10.1007/s00585-999-0190-6
- Cathey, E. H. (1969). Some midlatitude sporadic-e results from the explorer 20 satellite. *Journal of Geophysical Research* (1896-1977), 74(9), 2240–2247. https://doi.org/10.1029/JA074j009p02240
- Chandra, H., & Rastogi, R. G. (1975). Blanketing sporadic e layer near the magnetic equator. *Journal of Geophysical Research* (1896-1977), 80(1), 149–153. https://doi.org/10.1029/JA080i001p00149
- Chartier, A. T., Hanley, T. R., & Emmons, D. J. (2022). Long-distance propagation of 162 mhz shipping information links associated with
- sporadic e. Atmospheric Measurement Techniques, 15(21), 6387–6393. https://doi.org/10.5194/amt-15-6387-2022 Chimonas, G., & Axford, W. I. (1968). Vertical movement of temperate-zone sporadic e layers. Journal of Geophysical Research (1896-1977),
- 73(1), 111–117. https://doi.org/10.1029/JA073i001p00111
 Chisham, G., & Freeman, M. P. (2013). A reassessment of superdarn meteor echoes from the upper mesosphere and lower thermosphere. *Journal*
- Chisham, G., & Freeman, M. P. (2013). A reassessment of superdarn meteor echoes from the upper mesosphere and lower thermosphere. *Journal of Atmospheric and Solar-Terrestrial Physics*, 102, 207–221. https://doi.org/10.1016/j.jastp.2013.05.018
- Chisham, G., Lester, M., Milan, S., Freeman, M., Bristow, W., Grocott, A., et al. (2007). A decade of the super dual auroral radar network (superdarn): Scientific achievements, new techniques and future directions. *Surveys in Geophysics*, 28(1), 33–109. https://doi.org/10.1007/s10712-007-9017-8
- Christakis, N., Haldoupis, C., Zhou, Q., & Meek, C. (2009). Seasonal variability and descent of mid-latitude sporadic e layers at arecibo. *Annales Geophysicae*, 27(3), 923–931. https://doi.org/10.5194/angeo-27-923-2009
- Chu, Y. H., Wang, C. Y., Wu, K. H., Chen, K. T., Tzeng, K. J., Su, C. L., et al. (2014). Morphology of sporadic e layer retrieved from cosmic gps radio occultation measurements: Wind shear theory examination. *Journal of Geophysical Research: Space Physics*, 119(3), 2117–2136. https://doi.org/10.1002/2013JA019437
- Coleman, C. J. (1998). A ray tracing formulation and its application to some problems in over-the-horizon radar. Radio Science, 33(4), 1187–1197. https://doi.org/10.1029/98RS01523
- Davis, R. N., Du, J., Smith, A. K., Ward, W. E., & Mitchell, N. J. (2013). The diurnal and semidiurnal tides over ascension island and their interaction with the stratospheric quasi-biennial oscillation: Studies with meteor radar, ecmam and waccm. *Atmospheric Chemistry and Physics*, 13(18), 9543–9564. https://doi.org/10.5194/acp-13-9543-2013
- De Larquier, S., Ponomarenko, P., Ribeiro, A. J., Ruohoniemi, J. M., Baker, J. B. H., Sterne, K. T., & Lester, M. (2013). On the spatial distribution of decameter–scale subauroral ionospheric irregularities observed by superdarn radars. *Journal of Geophysical Research: Space Physics*, 118(8), 5244–5254. https://doi.org/10.1002/jgra.50475
- De Larquier, S., Ruohoniemi, J. M., Baker, J. B. H., Ravindran Varrier, N., & Lester, M. (2011). First observations of the midlatitude evening anomaly using super dual auroral radar network (superdarn) radars. *Journal of Geophysical Research*, 116(A10). https://doi.org/10.1029/2011JA016787
- Didebulidze, G. G., Dalakishvili, G., & Todua, M. (2020). Formation of multilayered sporadic e under an influence of atmospheric gravity waves (agws). Atmosphere, 11(6), 653. https://doi.org/10.3390/atmos11060653
- Drob, D. P., Emmert, J. T., Meriwether, J. W., Makela, J. J., Doornbos, E., Conde, M., et al. (2015). An update to the horizontal wind model (hwm): The quiet time thermosphere. *Earth and Space Science*, 2(7), 301–319. https://doi.org/10.1002/2014EA000089
- Earle, G. D., Kane, T. J., Pfaff, R. F., & Bounds, S. R. (2000). Ion layer separation and equilibrium zonal winds in midlatitude sporadic e. Geophysical Research Letters, 27(4), 461–464. https://doi.org/10.1029/1999GL900572
- Emmert, J. T., Drob, D. P., Picone, J. M., Siskind, D. E., Jones, M., Jr., Mlynczak, M. G., et al. (2021). Nrlmsis 2.0: A whole-atmosphere empirical model of temperature and neutral species densities. Earth and Space Science, 8(3), e2020EA001321. https://doi.org/10.1029/2020EA001321
- Evans, J. (1972a). Ionospheric movements measured by incoherent scatter: A review. Journal of Atmospheric and Terrestrial Physics, 34(2), 175–209. https://doi.org/10.1016/0021-9169(72)90164-X
- Evans, J. V. (1972b). Measurements of horizontal drifts in the e and f regions at millstone hill. *Journal of Geophysical Research* (1896-1977), 77(13), 2341–2352. https://doi.org/10.1029/JA077i013p02341
- Evans, J. V. (1978). Incoherent scatter contributions to studies of the dynamics of the lower thermosphere. *Reviews of Geophysics*, 16(2), 195–216. https://doi.org/10.1029/RG016i002p00195
- Feng, W., Marsh, D. R., Chipperfield, M. P., Janches, D., Höffner, J., Yi, F., & Plane, J. M. C. (2013). A global atmospheric model of meteoric iron. *Journal of Geophysical Research: Atmospheres*, 118(16), 9456–9474. https://doi.org/10.1002/jgrd.50708
- Galkin, I. A., Khmyrov, G. M., Kozlov, A. V., Reinisch, B. W., Huang, X., Paznukhov, V. V., et al. (2008). The artist 5. AIP Conference Proceedings, American Institute of Physics, 974, 150–159. https://doi.org/10.1063/1.2885024
- Galkin, I. A., Reinisch, B. W., & Bilitza, D. (2018). Realistic ionosphere: Real-time ionosonde service for ISWI. Sun and Geosphere, 13, 173–178. https://doi.org/10.31401/SunGeo.2018.02.09
- Goncharenko, L. P., & Salah, J. E. (1998). Climatology and variability of the semidiurnal tide in the lower thermosphere over millstone hill. Journal of Geophysical Research, 103(A9), 20715–20726. https://doi.org/10.1029/98JA01435
- $Haldoupis, C. (2011). \ A \ tutorial \ review \ on \ sporadic \ E \ layers \ (pp. 381-394). \ Springer \ Netherlands. \ https://doi.org/10.1007/978-94-007-0326-1_29$

KUNDURI ET AL. 12 of 14

21699402, 2023, 9, Downloaded from

.com/doi/10.1029/2023JA031455, Wiley Online Library on [11/07/2024]. See the Terms

- Haldoupis, C. (2012). Midlatitude sporadic e. a typical paradigm of atmosphere-ionosphere coupling. Space Science Reviews, 168(1), 441-461. https://doi.org/10.1007/s11214-011-9786-8
- Haldoupis, C., Meek, C., Christakis, N., Pancheva, D., & Bourdillon, A. (2006). Ionogram height-time-intensity observations of descending sporadic e layers at mid-latitude. Journal of Atmospheric and Solar-Terrestrial Physics, 68(3), 539-557. https://doi.org/10.1016/j. jastp.2005.03.020
- Haldoupis, C., Pancheva, D., & Mitchell, N. J. (2004). A study of tidal and planetary wave periodicities present in midlatitude sporadic e layers. Journal of Geophysical Research, 109(A2). https://doi.org/10.1029/2003JA010253
- Haldoupis, C., Pancheva, D., Singer, W., Meek, C., & MacDougall, J. (2007). An explanation for the seasonal dependence of midlatitude sporadic e layers. Journal of Geophysical Research, 112(A6), a-n. https://doi.org/10.1029/2007JA012322
- Hall, G. E., MacDougall, J. W., Moorcroft, D. R., St.-Maurice, J.-P., Manson, A. H., & Meek, C. E. (1997). Super dual auroral radar network observations of meteor echoes, Journal of Geophysical Research, 102(A7), 14603–14614, https://doi.org/10.1029/97JA00517
- Hall, S., McDonald, D., McGratten, G., & MacKenzie, E. (1971). Rocket observations of middle latitude sporadic e, magnetic fields, winds and ionization. Planetary and Space Science, 19(10), 1319-1325. https://doi.org/10.1016/0032-0633(71)90186-3
- Hodos, T. J., Nava, O. A., Dao, E. V., & Emmons, D. J. (2022). Global sporadic-e occurrence rate climatology using gps radio occultation and ionosonde data. Journal of Geophysical Research: Space Physics, 127(12), e2022JA030795. https://doi.org/10.1029/2022JA030795
- Hysell, D., Larsen, M., Fritts, D., Laughman, B., & Sulzer, M. (2018). Major upwelling and overturning in the mid-latitude f region ionosphere. Nature Communications, 9(1), 1–11, https://doi.org/10.1038/s41467-018-05809-x
- Hysell, D. L., Munk, J., & McCarrick, M. (2014). Sporadic e ionization layers observed with radar imaging and ionospheric modification. Geophysical Research Letters, 41(20), 6987-6993. https://doi.org/10.1002/2014GL061691
- Hysell, D. L., Nossa, E., Larsen, M. F., Munro, J., Sulzer, M. P., & González, S. A. (2009). Sporadic e laver observations over arecibo using coherent and incoherent scatter radar: Assessing dynamic stability in the lower thermosphere. Journal of Geophysical Research, 114(A12). https://doi.org/10.1029/2009JA014403
- Hysell, D. L., Yamamoto, M., & Fukao, S. (2002). Simulations of plasma clouds in the midlatitude e region ionosphere with implications for type i and type ii quasiperiodic echoes. Journal of Geophysical Research, 107(A10), 1313. SIA 17-1–SIA 17-9. https://doi.org/10.1029/2002JA009291
- Janches, D., Heinselman, C. J., Chau, J. L., Chandran, A., & Woodman, R. (2006). Modeling the global micrometeor input function in the upper atmosphere observed by high power and large aperture radars. Journal of Geophysical Research, 111(A7), A07317. https://doi. org/10.1029/2006JA011628
- Kopp, E. (1997). On the abundance of metal ions in the lower ionosphere. Journal of Geophysical Research, 102(A5), 9667–9674. https://doi. org/10.1029/97JA00384
- Krall, J., Huba, J. D., Nossa, E., Aponte, N., & Drob, D. P. (2020). Sami3 simulations of ionospheric metallic layers at arecibo. Journal of Geophysical Research: Space Physics, 125(3), e2019JA027297, https://doi.org/10.1029/2019JA027297
- Kunduri, B. S. R., Baker, J. B. H., Ruohoniemi, J. M., Thomas, E. G., & Shepherd, S. G. (2022). An examination of superdarn backscatter modes $using \ machine \ learning \ guided \ by \ ray-tracing. \ \textit{Space Weather}, \ 20(9), \ e2022SW003130. \ https://doi.org/10.1029/2022SW003130. \ https://doi.org/10.1$
- Larsen, M. F. (2000). A shear instability seeding mechanism for quasiperiodic radar echoes. Journal of Geophysical Research, 105(A11), 24931-24940. https://doi.org/10.1029/1999JA000290
- Larsen, M. F., Hysell, D. L., Zhou, Q. H., Smith, S. M., Friedman, J., & Bishop, R. L. (2007). Imaging coherent scatter radar, incoherent scatter radar, and optical observations of quasiperiodic structures associated with sporadic e layers. Journal of Geophysical Research, 112(A6), a-n.
- Lau, E. M., Avery, S. K., Avery, J. P., Janches, D., Palo, S. E., Schafer, R., & Makarov, N. A. (2006). Statistical characterization of the meteor trail distribution at the south pole as seen by a vhf interferometric meteor radar. Radio Science, 41(4), a-n. https://doi.org/10.1029/2005RS003247 Lehtinen, M. S., & Häggström, I. (1987). A new modulation principle for incoherent scatter measurements. Radio Science, 22(4), 625-634.
- https://doi.org/10.1029/rs022i004p00625 Lindzen, R. S., & Chapman, S. (1969). Atmospheric tides. Space Science Reviews, 10(1), 3-188. https://doi.org/10.1007/BF00171584
- Liu, Y., Zhou, C., Tang, Q., Li, Z., Song, Y., Qing, H., et al. (2018). The seasonal distribution of sporadic e layers observed from radio occultation measurements and its relation with wind shear measured by timed/tidi. Advances in Space Research, 62(2), 426-439. https://doi.org/10.1016/j.
- Maeda, J., & Heki, K. (2014). Two-dimensional observations of midlatitude sporadic e irregularities with a dense gps array in Japan. Radio Science, 49(1), 28-35. https://doi.org/10.1002/2013RS005295
- Maeda, J., & Heki, K. (2015). Morphology and dynamics of daytime mid-latitude sporadic-e patches revealed by gps total electron content observations in Japan. Earth Planets and Space, 67(1), 1-9. https://doi.org/10.1186/s40623-015-0257-4
- Mathews, J. (1998). Sporadic e: Current views and recent progress. Journal of Atmospheric and Solar-Terrestrial Physics, 60(4), 413-435. https:// doi.org/10.1016/S1364-6826(97)00043-6
- Matsushita, S., & Reddy, C. A. (1967). A study of blanketing sporadic e at middle latitudes. Journal of Geophysical Research (1896-1977), 72(11), 2903-2916. https://doi.org/10.1029/JZ072i011p02903
- Merriman, D. K., Nava, O. A., Dao, E. V., & Emmons, D. J. (2021). Comparison of seasonal foes and fbes occurrence rates derived from global digisonde measurements. Atmosphere, 12(12), 1558. https://doi.org/10.3390/atmos12121558
- Miller, K. L., & Smith, L. G. (1975). Horizontal structure of midlatitude sporadic-e layers observed by incoherent scatter radar. Radio Science, 10(3), 271–276, https://doi.org/10.1029/RS010i003p00271
- Nishitani, N., Ruohoniemi, J. M., Lester, M., Baker, J. B. H., Koustov, A. V., Shepherd, S. G., et al. (2019). Review of the accomplishments of mid-latitude super dual auroral radar network (superdarn) hf radars. Progress in Earth and Planetary Science, 6(1), 1-57. https://doi. org/10.1186/s40645-019-0270-5
- Obenberger, K. S., Dowell, J., Fallen, C. T., Holmes, J. M., Taylor, G. B., & Varghese, S. S. (2021). Using broadband radio noise from power-lines to map and track dense es structures. Radio Science, 56(2), e2020RS007169. https://doi.org/10.1029/2020RS007169
- Otsuka, Y., Tani, T., Tsugawa, T., Ogawa, T., & Saito, A. (2008). Statistical study of relationship between medium-scale traveling ionospheric disturbance and sporadic e layer activities in summer night over Japan. Journal of Atmospheric and Solar-Terrestrial Physics, 70(17), 2196-2202. https://doi.org/10.1016/j.jastp.2008.07.008
- Pezzopane, M., Scotto, C., Tomasik, Ł., & Krasheninnikov, I. (2010), Autoscala: An aid for different ionosondes, Acta Geophysica, 58(3), 513-526. https://doi.org/10.2478/s11600-009-0038-1
- Rawer, K. (1949). Measurement of sporadic e-layer Ionization. Nature, 163(4144), 528-529. https://doi.org/10.1038/163528a0
- Reinisch, B. W., & Galkin, I. A. (2011). Global ionospheric radio observatory (giro). Earth Planets and Space, 63(4), 377-381. https://doi. org/10.5047/eps.2011.03.001

KUNDURI ET AL. 13 of 14

- Roddy, P. A., Earle, G. D., Swenson, C. M., Carlson, C. G., & Bullett, T. W. (2007). The composition and horizontal homogeneity of e region plasma layers. *Journal of Geophysical Research*, 112(A6), a-n. https://doi.org/10.1029/2006JA011713
- Ruohoniemi, J. M., Greenwald, R. A., Baker, K. B., Villain, J. P., & McCready, M. A. (1987). Drift motions of small-scale irregularities in the high-latitude f region: An experimental comparison with plasma drift motions. *Journal of Geophysical Research*, 92(A5), 4553–4564. https:// doi.org/10.1029/JA092iA05p04553
- Schunk, R., & Nagy, A. (2009). Ionospheres: Physics, plasma physics, and chemistry. Cambridge University Press.
- Shinagawa, H., Tao, C., Jin, H., Miyoshi, Y., & Fujiwara, H. (2021). Numerical prediction of sporadic e layer occurrence using gaia. *Earth Planets and Space*, 73(1), 1–18. https://doi.org/10.1186/s40623-020-01330-y
- Singer, W., Von Zahn, U., & Weiß, J. (2004). Diurnal and annual variations of meteor rates at the arctic circle. Atmospheric Chemistry and Physics, 4(5), 1355–1363. https://doi.org/10.5194/acp-4-1355-2004
- Smith, L. G. (1966). Rocket observations of sporadic e and related features of the e region. *Radio Science*, 1(2), 178–186. https://doi.org/10.1002/rds196612178
- Wand, R. H. (1983). Geomagnetic activity effects on semidiurnal winds in the lower thermosphere. *Journal of Geophysical Research*, 88(A11), 9243–9248. https://doi.org/10.1029/JA088iA11p09243
- Whitehead, J. (1961). The formation of the sporadic-e layer in the temperate zones. *Journal of Atmospheric and Terrestrial Physics*, 20(1), 49–58. https://doi.org/10.1016/0021-9169(61)90097-6
- Whitehead, J. (1989). Recent work on mid-latitude and equatorial sporadic-e. *Journal of Atmospheric and Terrestrial Physics*, 51(5), 401–424. https://doi.org/10.1016/0021-9169(89)90122-0
- Wilkinson, P. J., Szuszczewicz, E. P., & Roble, R. G. (1992). Measurements and modelling of intermediate, descending, and sporadic layers in the lower ionosphere: Results and implications for global-scale ionospheric-thermospheric studies. *Geophysical Research Letters*, 19(2), 95–98. https://doi.org/10.1029/91GL02774
- Wu, D. L., Ao, C. O., Hajj, G. A., De la Torre Juarez, M., & Mannucci, A. J. (2005). Sporadic e morphology from gps-champ radio occultation. Journal of Geophysical Research, 110(A1), A01306. https://doi.org/10.1029/2004JA010701
- Yamamoto, M., Fukao, S., Ogawa, T., Tsuda, T., & Kato, S. (1992). A morphological study on mid-latitude e-region field-aligned irregularities observed with the mu radar. *Journal of Atmospheric and Terrestrial Physics*, 54(6), 769–777. https://doi.org/10.1016/0021-9169(92)90115-2
- Yamazaki, Y., Arras, C., Andoh, S., Miyoshi, Y., Shinagawa, H., Harding, B. J., et al. (2022). Examining the wind shear theory of sporadic e with icon/mighti winds and cosmic-2 radio occultation data. *Geophysical Research Letters*, 49(1), e2021GL096202. https://doi.org/10.1029/2021GL096202
- Yu, B., Xue, X., Scott, C. J., Wu, J., Yue, X., Feng, W., et al. (2021). Interhemispheric transport of metallic ions within ionospheric sporadic e layers by the lower thermospheric meridional circulation. Atmospheric Chemistry and Physics, 21(5), 4219–4230. https://doi.org/10.5194/ acp-21-4219-2021
- Zeng, Z., & Sokolovskiy, S. (2010). Effect of sporadic e clouds on gps radio occultation signals. *Geophysical Research Letters*, 37(18), a-n. https://doi.org/10.1029/2010GL044561

KUNDURI ET AL. 14 of 14